

Final Technical Report

USGS Award Number

G20AP00053

Title of Award

Characterization of Nonlinear Dynamic Soil
Properties from Geotechnical Downhole
Array Data

Authors

Ertugrul Taciroglu
University of California at Los Angeles
5731 Boelter Hall
Los Angeles, CA 90095
310-267-4655 (Tel.)
etacir@ucla.edu

S. Farid Ghahari
University of California at Los Angeles
4731 Boelter Hall
Los Angeles, CA 90095
ghahari@seas.ucla.edu

Term Covered by the Award:

06/01/2020 to 05/31/2021

Acknowledgment of Support

The authors would like to acknowledge Prof. Pedro Arduino from the University of Washington for his fruitful comments and OpenSees implementation of the “BA” model. In addition, the contributions of Prof. Hamed Ebrahimian, Dr. Wenyang Zhang, and Dr. Fariba Abazarsa are greatly appreciated. This work was supported by the U.S. Geological Survey (USGS) via the External Research Program award G20AP00053.

Disclaimer

The views and conclusions contained in this document are those of the authors and should not be interpreted as representing the opinions or policies of the U.S. Geological Survey. Mention of trade names or commercial products does not constitute their endorsement by the U.S. Geological Survey.

Abstract

Nonlinear soil responses manifested through site and soil-structure interaction effects must be taken into account to accurately predict the response of civil structures under earthquake excitations. The nonlinear properties of soil layers must, therefore, be accurately and reliably estimated. Identifying these parameters from earthquake data recorded by geotechnical arrays is a promising solution because such data represent a full-scale experiment replete with every detail. In this project, we devise a stochastic filtering framework to estimate nonlinear soil properties from such data. To do so, a one-dimensional Finite Element Model of a site is modeled, and the parameters of the soil's constitutive model together with the input excitation (incident, bedrock, or "within" motions) are identified using Unscented Kalman Filter techniques. The devised method is verified using several synthetic examples and validated using centrifuge test data and event data recorded at the well-known Lotung site. The method is also applied to earthquake data recorded by several CSMIP Geotechnical Arrays—only one of which is presented here for brevity.

1 Introduction

Although near-surface probable nonlinear soil layers have a negligible dimension compared to the path seismic waves passed from the source to the site, they significantly contribute to the observed ground motion on the ground surface [1]. So, realistic physics-based predictions could not be achieved unless the effects of the near-surface nonlinear soil are taken into account. While there are quite a number of veritable analytical and numerical methods to predict site response given bedrock or outcrop motions (for example, [2]–[4]), their accuracies inherently depend on the knowledge of the soil layers dynamic properties. However, laboratory testing of "undisturbed" soil samples inevitably involves some violation of in-situ conditions. For example, loading paths in the lab tests are significantly different from those that the soil experiences in the field. To resolve this problem, field measurements had been suggested. Cross-Hole Tests (CHT), Down-Hole Tests (DHT), Suspension Logging, Seismic Reflection, Seismic Refraction, and Spectral Analysis of Surface Waves (SASW) are among various methods that are used for measuring shear wave velocities of soil layers, which is a key parameter for predicting the linear dynamic responses of a soil deposit. However, even these in-situ tests cannot mimic the actual behavior of the site under real-life earthquakes. This is because the sources of real-life seismic waves are different from those used in in-situ tests. Moreover, in-situ tests are typically only able to capture the very-small-strain (and thus linear) responses of the soil layers. On the other hand, it is well accepted that soil mostly behaves nonlinearly during even moderate earthquakes and reaches strains well beyond those that can be induced in conventional in-situ tests [5].

Not surprisingly, the estimation of dynamic site properties from recorded ground motions has been an important topic of research (for example, [6], [7]), because earthquakes may be regarded as prototype in-situ dynamic tests carried out by nature and the data recorded during earthquakes offer precious opportunities for the study of in-situ behavior of soil within a strain range that has engineering significance. However, most of the identification studies carried out in the past are limited to linear or equivalent linear soil properties of soil layers [8], [9]. These limited studies, in which soil nonlinearity was considered, have limited applicability because the assumed constitutive nonlinear model was very simple [10]. Moreover, in many such studies, in-depth motions were used as input excitations through the conventional outcrop method (with absorbing boundary condition), which reduces the applicability range of the method. More importantly, it is well accepted that *within* motions are polluted by downgoing waves and should not be used as outcrop input excitations [11].

In this project, we propose an inverse solution that significantly mentioned the above limitations. As schematically shown in **Figure 1**, considering one-dimensional (1D) site response and having general information like layering and soil types, we develop, test, and validate input-output and output-only identification algorithms to identify nonlinear soil properties, as well as incident motions, from data

recorded in a geotechnical array. The current version of the proposed solution needs a reasonable initial guess for soil parameters. Also, a specific nonlinear constitutive model is used while the extension of the method to study the plausibility of various models is straightforward.

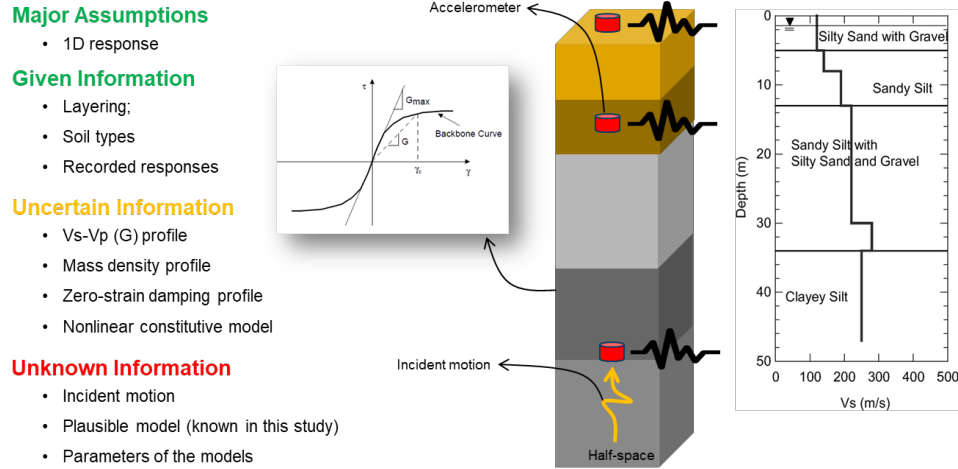


Figure 1. The level of information needed or estimated in this project.

2 The Proposed Framework

There are two approaches to carry out dynamic site response analyses, as shown in **Figure 2**. In the more traditional approach, the site is modeled up to the bedrock depth (half-space), and the radiation damping is modeled by using an absorbing boundary to prevent wave reflections. Through this approach, the incident motion must be used as input excitation, which is theoretically can be obtained from nearby rock outcrop motion (with a $\frac{1}{2}$ factor). However, as seen, this approach is only valid if there is no impedance contrast below the boundary level and there is a very close rock outcrop motion. In another approach, the domain can be cut at any depth as long as the so-called within motion (measured in-depth motion) is used as input excitation, and a fixed boundary is used.

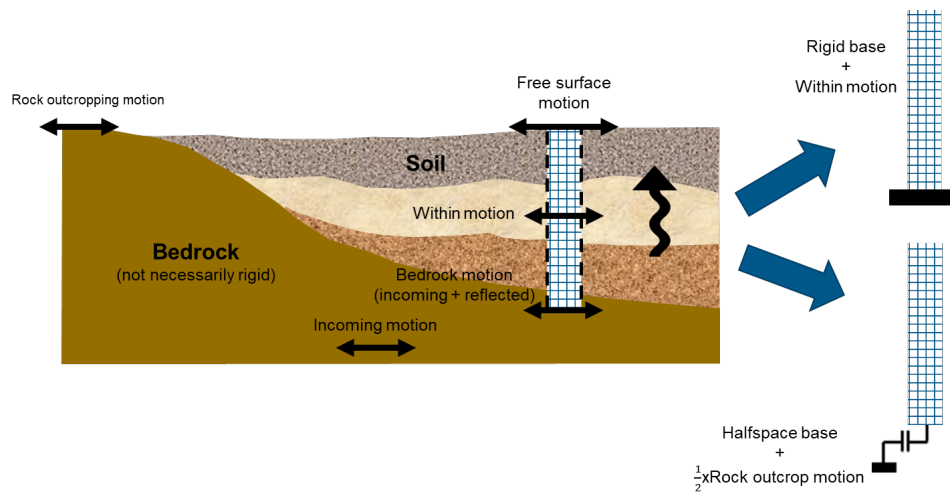


Figure 2. One-dimensional site analysis approaches.

We propose to solve the inverse problem using output-only sequential Bayesian estimation [12]–[14], as shown in **Figure 3**. In this approach, the 1D FE model of the site is modeled up to the bedrock depth with an absorbing boundary condition if the bedrock is not rigid. Then, a soil constitutive model is chosen, and its parameters are identified along with the unknown incident motion through a Bayesian model updating approach, details of which are presented in the next section.

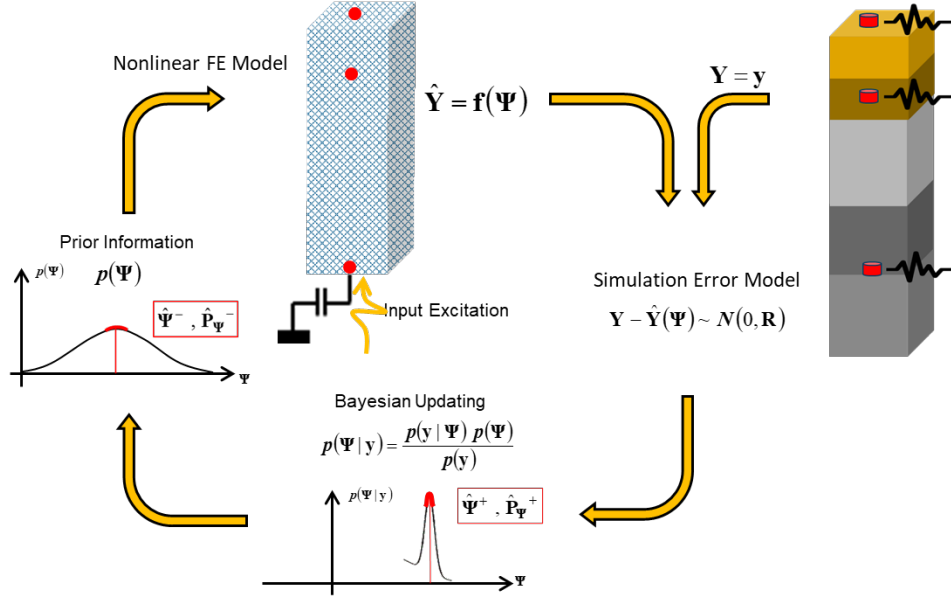


Figure 3. The one-step solution.

The aforementioned joint input-parameter estimation solution is prone to a large uncertainty level if the number of parameters is large or the number of in-depth recorded data is limited. To resolve this issue, we classify all possible problems into five classes as schematically shown in **Figure 4** depending on the real bedrock condition, the complexity of the domain, and the location of the sensors. The simplest problem is one with a few layers and multiple sensors, a rigid bedrock, and a sensor at the bedrock (**Figure 4a**). In these types of problems, we will use the Input-Output (IO) version of the identification algorithm to estimate the soil's material model parameters. If the domain gets complicated, but there is still a sensor at the bedrock, and the bedrock is rigid, the IO identification is the best strategy (**Figure 4b**).

On the other hand, if the domain is simple, but there is no sensor at the bedrock depth (**Figure 4c**), while the Output-Only (OO) version of the algorithm can work, a two-step method will be another option. In the two-step method, the domain is assumed fixed at the deepest instrumented point, and the IO identification method is used to estimate the parameters of the domain. Then, in the second step, the identification method in the OO setting is employed to estimate the remaining parameters (if any) as well as incident motion. The same strategy can be used for a simple domain on top of the non-rigid half-space if there is a sensor at the bedrock depth (**Figure 4d**). However, if the domain is complex, the output-only solution cannot work because there would be a large list of uncertain parameters and input excitations. In these problems (**Figure 4e**), only the 2-step solution could work. Finally, similar to the previous case, if there is no sensor at the bedrock depth, but the bedrock is rigid, then the two-step solution is recommended (**Figure 4f**).

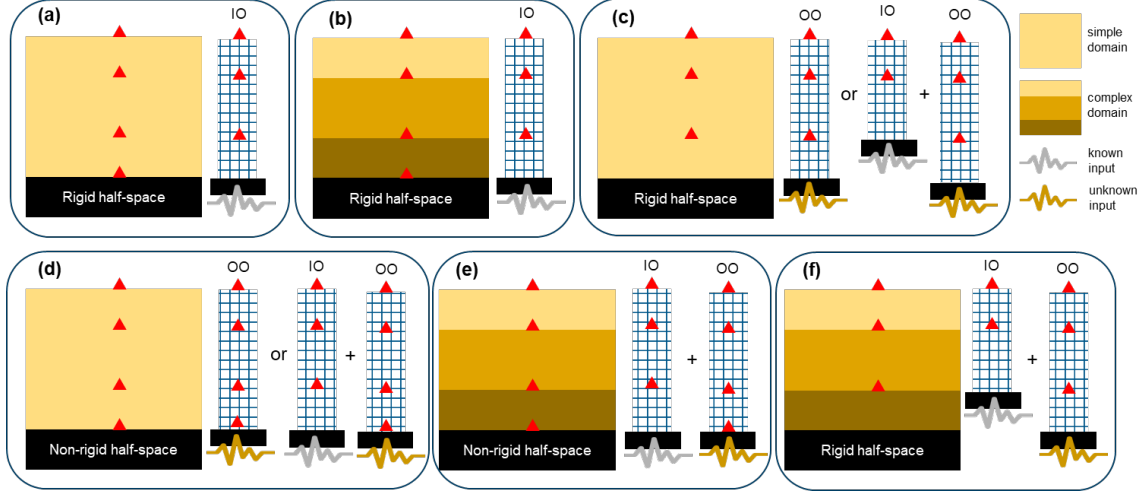


Figure 4. Various possible estimation problems. IO and OO represent the “Input-Output” and “Output-Only” identification methods, respectively.

2.1 The Bayesian Model Updating

Herein, Bayesian model updating is briefly reviewed. The formulation is presented for the general case of parameter-input estimation, and it is used here for parameter estimation in the IO mode.

Let’s assume a site with a soil deposit, as shown in Figure 5 (left). There are m soil layers located above an elastic half-space with finite rigidity (bedrock) and excited by vertically propagating earthquake excitations. Using a geotechnical array, absolute accelerations at several points (not necessarily at all layers or even boundaries of layers) are recorded. This continuous system can be modeled using a Finite Element (FE) model as shown in Figure 5 (right) [15], for example. Note that This model is a 1D-2C (two components) model with plane strain assumption, but the estimation method can be used for 1D-3C (three components) without any changes. To account for the finite rigidity of the bedrock, a Lysmer-Kuhlemeyer [16] dashpot is incorporated at the base of the soil column, whose coefficient equals the product of the mass density and shear wave velocity of the bedrock with the area of the base of the soil column (size of the element). The soil column is excited at the base by a horizontal force time-history, which is equal to the ground (outcrop motion) velocity multiplied by the dashpot’s coefficient [17].

The response of the FE model at each time step to the applied force time-history can be expressed as a nonlinear function of the model parameter vector, θ , and the time-history of the force, $\mathbf{f}_{1:i}$,

$$\hat{\mathbf{y}}_i = h_i(\theta, \mathbf{f}_{1:i}), \quad (1)$$

where $\theta = [\theta_1, \dots, \theta_{n_\theta}]$ contains n_θ parameters (e.g., the layers’ shear wave velocities, parameters of the constitutive models, etc.) that define the FE model, and $h_i(\cdot)$ is the nonlinear response function of the FE model at time step i , encapsulating all the dynamics of the model from time step 1 to i . The measured response vector of the site, \mathbf{y}_i , is related to the FE predicted response, $\hat{\mathbf{y}}_i$, as

$$\mathbf{v}_i(\theta, \mathbf{f}_{1:i}) = \mathbf{y}_i - \hat{\mathbf{y}}_i(\theta, \mathbf{f}_{1:i}), \quad (2)$$

where $\mathbf{v}_i \in \mathbb{R}^{n_y \times 1}$ is the simulation error vector that accounts for the misfit between the measured responses of the site at n_y locations and the FE-predicted response. The simulation error is ideally modeled as a zero-mean Gaussian white noise vector (i.e., $\mathbf{v}_i \sim N(\mathbf{0}, \mathbf{R})$) by neglecting the effects of modeling error. The objective of the estimation problem is to find the estimates of the unknown parameter vector, i.e., $\psi_i =$

$[\theta^T, f_{1:i}^T]^T$, for which the discrepancies between the measured and FE predicted responses are minimized in a probabilistic sense. Since the estimation problem is highly nonlinear, a sequential estimation approach is used to improve estimation efficiency. The time domain is divided into successive overlapping time windows in our approach, referred to as the estimation windows. The problem is then solved at each window to estimate the unknown parameter vector.

Assume that the m -th estimation window spans from time step t_1^m to time step t_2^m . Therefore, the unknown parameter vector at this estimation window is defined as $\psi_m = [\theta^T, f_{t_1^m:t_2^m}^T]^T$, where $\psi_m \in \mathbb{R}^{(n_\theta+t_l) \times 1}$, in which $t_l = t_2^m - t_1^m$ is the window length. The unknown parameter vector, ψ_m , can be estimated using a parameter-only Kalman filtering method (e.g., [18]). To this end, the unknown parameter vector is modeled as a random vector, the evolution of which is characterized by a Gaussian Markov process—also known as a random walk. Then, a state-space model is set up, in which the state equation governs the evolution of the random parameter vector and the measurement equation corresponds to the discrepancies between the measured and FE predicted responses [19], i.e.,

$$\psi_{m,k+1} = \psi_{m,k} + \gamma_{m,k}, \quad (3)$$

$$y_{t_1^m:t_2^m} = \hat{y}_{t_1^m:t_2^m,k+1}(\psi_{m,k+1}) + v_{t_1^m:t_2^m,k+1}, \quad (4)$$

where $\gamma_{m,k} \sim N(\mathbf{0}, \mathbf{Q})$, $v_{t_1^m:t_2^m,k+1} \sim N(\mathbf{0}, \tilde{\mathbf{R}})$, where $\tilde{\mathbf{R}} \in \mathbb{R}^{(t_l \times n_y) \times (t_l \times n_y)}$ is a block diagonal matrix, whose block diagonals are the simulation error covariance matrix \mathbf{R} . In Eqs. (3) and (4), k denotes the iteration number. As can be observed, the estimation process at each estimation window is iterative, i.e., the mean vector and covariance matrix of the unknown parameter vector is iteratively updated based on the discrepancies between the time histories of the measured and estimated responses.

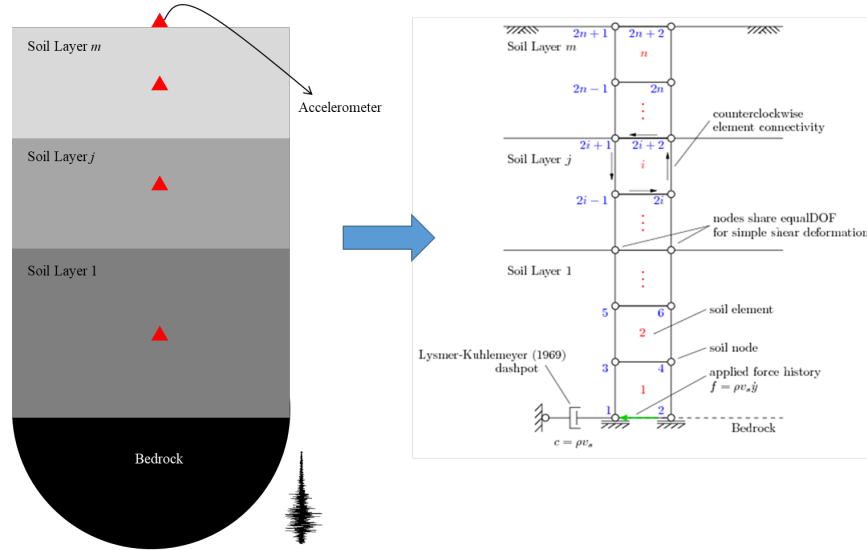


Figure 5. Instrumented soil deposit (left) and its equivalent discrete FE model (right) [15].

An Unscented Kalman Filtering (UKF) [20] method can then be used to update the unknown parameter vector at each iteration. In our method, the nonlinear FE model is evaluated separately at a set of deterministically selected realizations of the unknown parameter vector, which are referred to as the sigma points (SPs) denoted by θ^j . The sigma points are selected around the prior mean estimate $\hat{\psi}^-$. In this study, a scaled Unscented Transformation (UT) based on $2n_\psi + 1$ sigma points (i.e., $j = 1, 2, \dots, 2n_\psi + 1$) is used,

where n_ψ denotes the size of the extended parameter vector. The mean and covariance matrix of the FE predicted structural responses, and the cross-covariance matrix of ψ and y are respectively computed using a weighted sampling method as

$$\bar{y} = \sum_{j=1}^{2n_\psi+1} W_m^j \hat{y}_i(\boldsymbol{\vartheta}^j), \quad (5)$$

$$\hat{\mathbf{P}}_{yy} = \sum_{j=1}^{2n_\psi+1} W_e^j [\hat{y}_i(\boldsymbol{\vartheta}^j) - \bar{y}][\hat{y}_i(\boldsymbol{\vartheta}^j) - \bar{y}]^T + \mathbf{R}, \quad (6)$$

$$\hat{\mathbf{P}}_{\psi y} = \sum_{j=1}^{2n_\psi+1} W_e^j [\boldsymbol{\vartheta}^j - \hat{\psi}^-][\hat{y}_i(\boldsymbol{\vartheta}^j) - \bar{y}]^T, \quad (7)$$

where W_m^j and W_e^j denote weighting coefficients [20]. Now, the UKF prediction-correction procedure can be employed to estimate the posterior parameter mean vector $\hat{\psi}_{m,k+1}^+$ and covariance matrix $\hat{\mathbf{P}}_{\psi,m,k+1}^+$ at each iteration. The proposed identification algorithm is summarized in Table 1.

Table 1. Identification algorithm for joint estimation of the model parameters and the FIM time history.

<p>1. Set the estimation window length t_l, and the start and end points of each estimation window.</p> <p>2. Set the initial mean vector and covariance matrix of the unknown parameter vector as</p> $\hat{\psi}_0^+ = [\hat{\theta}_0^T, \mathbf{f}_{t_1^0:t_2^0}^0]^T, \text{ and } \mathbf{P}_{\psi,0}^+ = \begin{bmatrix} \hat{\mathbf{P}}_{\theta\theta,0} & \mathbf{0} \\ \mathbf{0} & \hat{\mathbf{P}}_{f^0} \end{bmatrix}.$ <p>3. Define the process noise covariance matrix \mathbf{Q} and the simulation error covariance matrix \mathbf{R}. Set up matrix $\tilde{\mathbf{R}}$.</p> <p>4. For the m-th estimation window:</p> <p>4.1. Retrieve the posterior estimates of the mean vector and covariance matrix of the unknown parameter vector from the last estimation window (i.e., $\hat{\psi}_{m-1}^+$, and $\mathbf{P}_{\psi,m-1}^+$). Set up $\hat{\psi}_{m,0}^+$ and $\mathbf{P}_{\psi,m,0}^+$ based on $\hat{\psi}_{m-1}^+$ and $\mathbf{P}_{\psi,m-1}^+$.</p> <p>4.2. Iterate ($k = 1, 2, \dots$):</p> <p>a. Set $\hat{\psi}_{m,k+1}^- = \hat{\psi}_{m,k}^+$, $\mathbf{P}_{\psi,m,k+1}^- = \mathbf{P}_{\psi,m,k}^+ + \mathbf{Q}$.</p> <p>b. Generate sigma points. Run the FE model for $(2n_\psi + 1)$ sigma points. Derive \bar{y}, $\hat{\mathbf{P}}_{yy}$, and $\hat{\mathbf{P}}_{\psi y}$ using Eqs. (5)-(7).</p> <p>c. Compute the Kalman gain matrix: $\mathbf{K} = \hat{\mathbf{P}}_{\psi y}(\hat{\mathbf{P}}_{yy})^{-1}$.</p> <p>d. Find the corrected estimates of the mean vector and covariance matrix of the unknown parameter vector: $\hat{\psi}_{m,k+1}^+ = \hat{\psi}_{m,k+1}^- + \mathbf{K}(\mathbf{y}_{t_1^m:t_2^m} - \bar{y})$, $\mathbf{P}_{\psi,m,k+1}^+ = \mathbf{P}_{\psi,m,k+1}^- - \mathbf{K}(\hat{\mathbf{P}}_{yy} + \tilde{\mathbf{R}})\mathbf{K}^T$.</p> <p>e. Check for convergence: if $\hat{\psi}_{m,k+1}^+ - \hat{\psi}_{m,k}^+ < 0.02 \times \hat{\psi}_{m,k-1}^+$ or $k + 1 > 10$, then move to the next estimation window ($m = m + 1$, go to step 4); otherwise, iterate again at the current estimation window ($k = k + 1$, go to step 4.2).</p>

2.2 The Selected Constitutive Model

During the last few decades, a broad range of nonlinear soil models—uniaxial to multi-axial, phenomenological to physics-based—have been devised (e.g., [21], [22], [23], [24], [25]). For example, one of the most well-known and advanced nonlinear soil models is the one devised by Elgamal and co-workers [25]. In that model, soil plasticity is formulated based on the multi-surface concept, with a non-associative flow rule to reproduce the well-known dilatancy effect. The yield surfaces are of the Drucker-Prager [26] type. This model is frequently used in the direct simulation of SSI problems within the research community and is already available in OpenSees [27]. The multiple hierarchical yield surfaces of this model enable it to approximate the soil behavior within a broad range of strain regimes, but this is also its disadvantage in that a large number of requisite model parameters renders the calibration process

formidable. By the same token, the model may exhibit spurious sensitivities. As we are going to solve a massive inverse problem using real-life data, these two major drawbacks are problematic.

A model with a simpler scaffold is that proposed by Borja and Amies [22]. This is also a multi-surface model but only has a bounding surface and a vanishing elastic region. Incidentally, the Borja-Amies (BA) model only needs a few parameters for calibration. The validity of this model was examined by utilizing the downhole array motions recorded at Lotung, Taiwan, through one-dimensional nonlinear site response analyses [28] with promising success. The model admits an additive decomposition of the stress into inviscid (frictional) and viscous parts, as in:

$$\boldsymbol{\sigma} = \boldsymbol{\sigma}^{inv} + \boldsymbol{\sigma}^{vis}, \quad \boldsymbol{\sigma}^{inv} = \mathbf{C}^e : (\boldsymbol{\epsilon} - \boldsymbol{\epsilon}^p), \quad \boldsymbol{\sigma}^{vis} = \mathbf{D} : \dot{\boldsymbol{\epsilon}} \quad (8)$$

where \mathbf{C}^e and \mathbf{D} are elastic stiffness and viscous damping tensors, respectively; $\boldsymbol{\epsilon}$ is the total strain tensor; $\boldsymbol{\epsilon}^p$ is the plastic strain tensor; and $\dot{\boldsymbol{\epsilon}}$ is the total strain rate. Given this decomposition, the model can also incorporate material level strain-rate-dependent damping, enabling a modeler to match field-identified damping behavior, even when such behavior is complex. Omitting details here for brevity, the main equation to calibrate this model is,

$$\frac{G}{G_{max}} = 1 - \frac{3}{2\tau_o} \int_0^{2\tau_o} \left[h \left(\frac{R/\sqrt{2} + \tau_o - \tau}{\tau} \right)^m + H_0 \right]^{-1} d\tau \quad (9)$$

where $G = \tau_o/\gamma_o$ is the secant shear stiffness, and R is the radius of the bounding surface, and parameters h , m and H_0 control the intensity of the hardening. The model can be directly calibrated using an experimentally obtained (or otherwise estimated from real-life) G/G_{max} curve [29] and a frequency-dependent damping curve. In the present study, we incorporate this model with the UKF-based estimation method described above.

The advantages of the BA model are clear:

- It is a thermodynamically consistent model based on the classical viscoplasticity framework with well-defined parameters.
- It is a three-dimensional model, and thus, if it is accurately calibrated, it can accurately predict soil behavior under multi-axial stress states, such as those due to irregular surface topography and soil stratigraphy, or underground scatterers.

As a part of a parallel study, the BA model has been successfully implemented in Opensees and extensively verified and validated [30]. In this study, we use Opensees [27] for all needed simulations, and the soil model is this recently implemented BA model.

3 Verification Using Synthetic Data

To verify the proposed inverse solution for the identification of nonlinear soil properties, four problems are designed and solved, which cover all cases presented in **Figure 4**. **Figure 6**(left) shows the profile of the site. It consists of four layers numbered from bottom to top. This 47 m site is on top of an elastic half-space which is replaced by a horizontal and vertical dashpot with coefficients¹ $c_h = \rho V_s$ and $c_v = \rho V_p$, respectively, in which ρ is the mass density of the half-space and V_s and V_p are, respectively, shear and compressional wave velocity of the half-space. The parameters defining the nonlinear BA model of all four

¹ This is a plane strain problem with both in plane and out of plane dimensions equal to 1 m.

layers are shown in this figure too. It is assumed that there are four accelerometers shown by red triangles in **Figure 6**(left) which record the response of the site under two vertically propagating shear and compressional excitations shown in red and green, respectively. To be realistic, vertical and North-South velocity records in 35 m depth at CSMIP (California Strong Motion Instrumentation Program) [31] station 68323 recorded during the 2014 South Napa earthquake are used as incident excitation. To make sure the site behaves nonlinearly under this input excitation, both components are magnified by a factor of 10, which results in an input excitation with a horizontal peak acceleration of $0.14g$. **Figure 6**(right) shows the scaled vertical and horizontal accelerations of these two input excitations. For the simulation and identification studies, 30 seconds of the significant portion of these signals is used, which is shown in **Figure 6**(left) by a red rectangle.

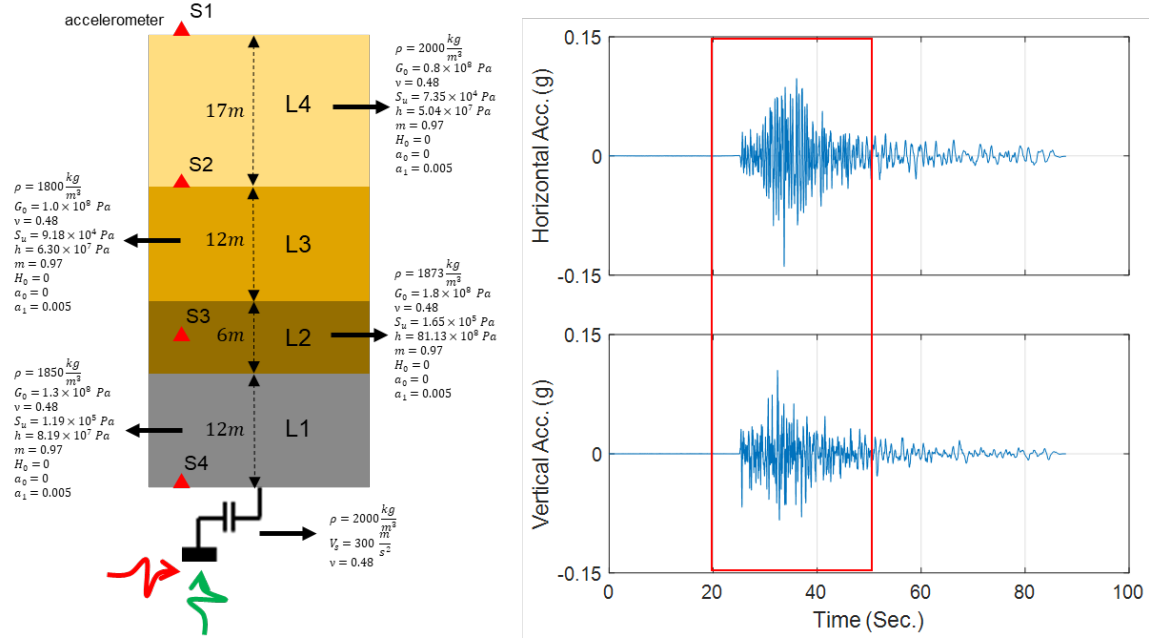


Figure 6. Soil profile used for the verification studies (left) and horizontal and vertical incident motions.

In all simulation-identification studies presented following a random noise with 5% RMS (Root Mean Squares) of the noise-free response signals are added to the simulated response to mimic real-life conditions.

3.1 Case 1: Complex Domain with Measured Incident/Outcrop Motion

In the first case, it is assumed that the incident motion is available, for example through outcrop measurement. So, the identification method is employed in the IO setting to estimate 5 parameters (G_0, S_u, h, m, a_1) for all four layers in one step. To do that, all four noisy measured horizontal acceleration responses are used. The identification begins with assuming a 30% initial error with respect to the true values shown in **Figure 6**(right). **Figure 7** shows the variation of estimated parameters (normalized with the corresponding true values) at every iteration. As seen in this figure, most of the parameters quickly converge to the true values once the moving window receives data from the strong portion of the data. There are some errors in identified parameters of the second layer, which is expected because its contribution to the response of the site is smaller due to its thickness. Specifically, the Rayleigh damping parameter (a_1) of this layer has little effects on the measured responses. To support this statement, **Figure 8** shows a comparison between measured (simulated) acceleration responses at four instrumented levels with the corresponding predictions obtained using final estimated parameters. As seen, predicted responses are identical to the measured (simulated) responses.

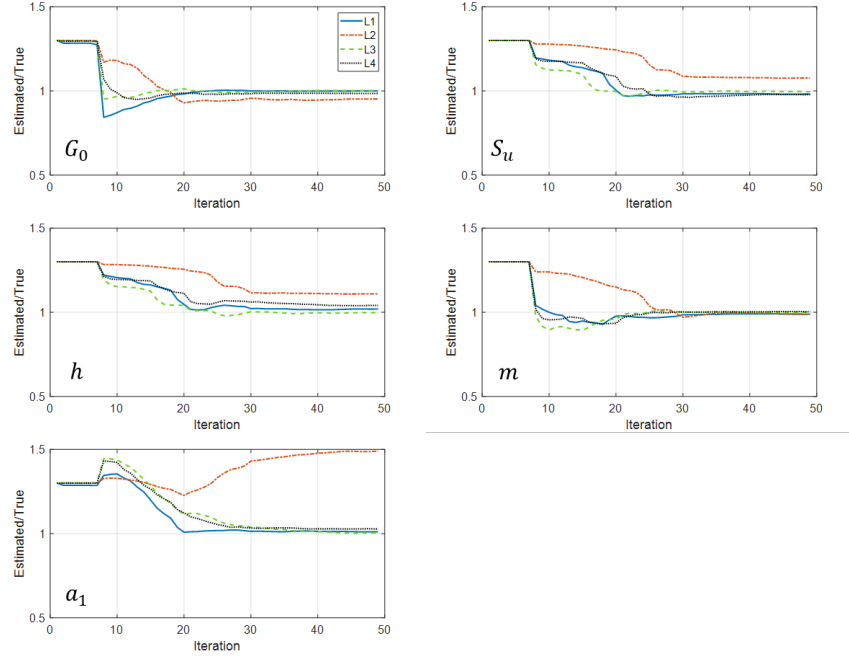


Figure 7. Identified parameters in Case 1 (normalized by the true values).

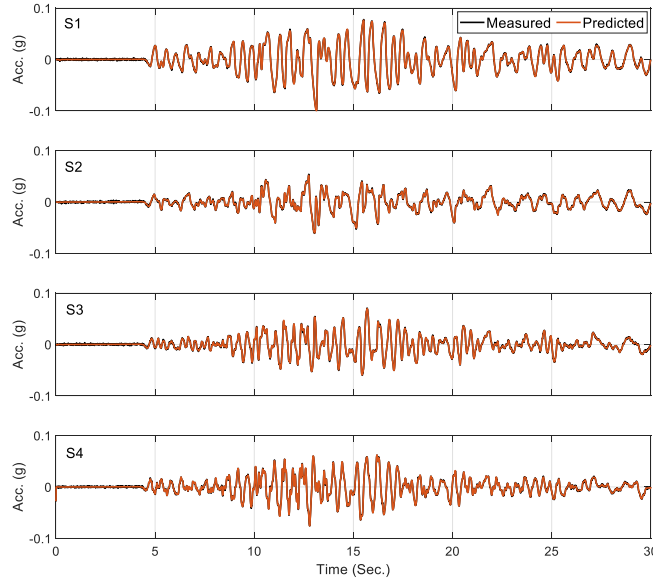


Figure 8. Comparison between measured and predicted acceleration responses in Case 1.

Finally, **Table 2** presents the final estimation error of all 20 parameters. As already observed in **Figure 7**, this table shows that all parameters are identified with high accuracy except a few parameters of the second layer, especially the Rayleigh damping parameter.

Table 2. The initial and final error of parameters in Case 1.

Layer	Parameter	Initial Error (%)	Final Error (%)
1	G_0	+30	0.04
	S_u	+30	-1.86
	h	+30	1.97
	m	+30	-1.16
	a_1	+30	1.04
2	G_0	+30	-4.72
	S_u	+30	7.64
	h	+30	10.91
	m	+30	-1.09
	a_1	+30	49.02
3	G_0	+30	0.24
	S_u	+30	-0.42
	h	+30	-0.19
	m	+30	0.02
	a_1	+30	0.32
4	G_0	+30	-1.40
	S_u	+30	-2.15
	h	+30	4.08
	m	+30	0.35
	a_1	+30	2.72

3.2 Case 2: Estimation of the Incident Motion For a Completely Known Site

In the second case, it is assumed that the site is fully known, and the identification method is employed in its OO mode to back-calculate the incident motion. For this step, because input estimation through the Kalman filter is prone to low-frequency error, velocity responses at S1 to S4 locations are also used along with the acceleration responses. **Figure 9** shows the comparison between the exact incident motion and the estimated motion. As seen, the estimated motion is almost identical to the exact record.

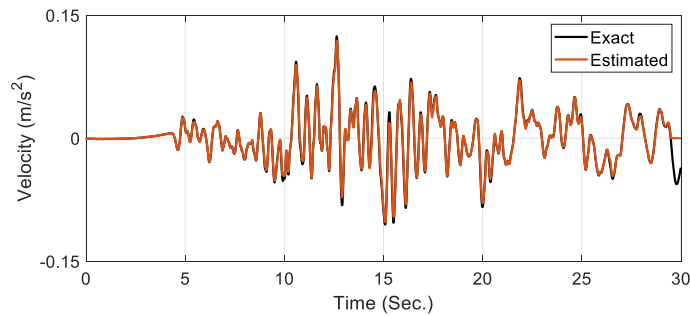


Figure 9. Comparison between the exact and estimated incident motion in Case 2.

3.3 Case 3: Simple Domain with Unknown Incident/Outcrop Motion

In the third case, the joint estimation of input and parameters are investigated. As mentioned before, if the domain is complex and therefore the number of updating parameters is large, the problem must be solved in two steps. This case will be presented in the next section. Herein, joint input-parameter estimation is carried out for a simple domain. The domain is a uniform soil layer with the same thickness (47 m) as the total thickness of the complex domain with $\rho = 1850 \frac{kg}{m^3}$, $G_0 = 1.3 \times 10^8 Pa$, $\nu = 0.48$, $S_u = 1.19 \times 10^5 Pa$, $h = 8.19 \times 10^7 Pa$, $m = 0.97$, $H_0 = 0$, $a_0 = 0$, $a_1 = 0.005$. The location of the sensors and the properties of the half-space are also the same as before. **Figure 10** shows the variation of estimated parameters (normalized with the corresponding true values) at every iteration. As seen in this figure, G_0 , h , and m converge to the true values, while there is a small error in S_u and as expected large error in a_1 . The comparison between the estimated and exact input excitation as well as measured (simulated) and predicted acceleration responses shown, respectively, in **Figure 11** and **Figure 12** confirm that the response of the system is not very sensitive to these parameters. Final errors in the estimated parameters are reported in **Table 3**.

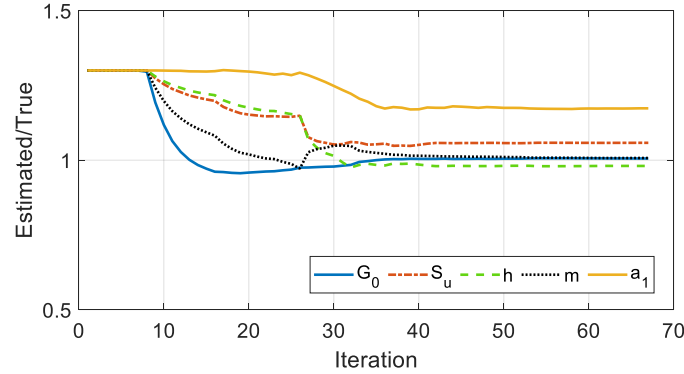


Figure 10. Identified parameters in Case 3 (normalized by the true values).

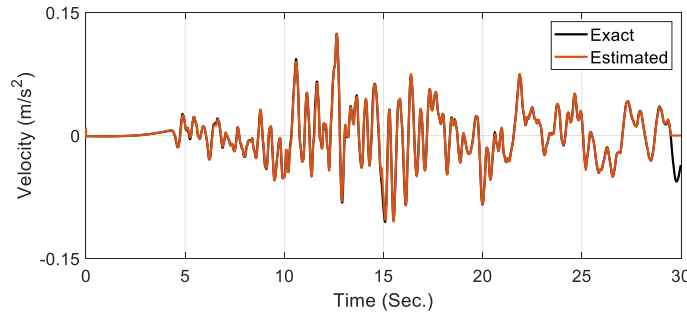


Figure 11. Comparison between the exact and estimated incident motion in Case 3.

Table 3. The initial and final error of parameters in Case 3.

Layer	Parameter	Initial Error (%)	Final Error (%)
1	G_0	+30	0.56
	S_u	+30	5.80
	h	+30	-1.92
	m	+30	0.71
	a_1	+30	17.33

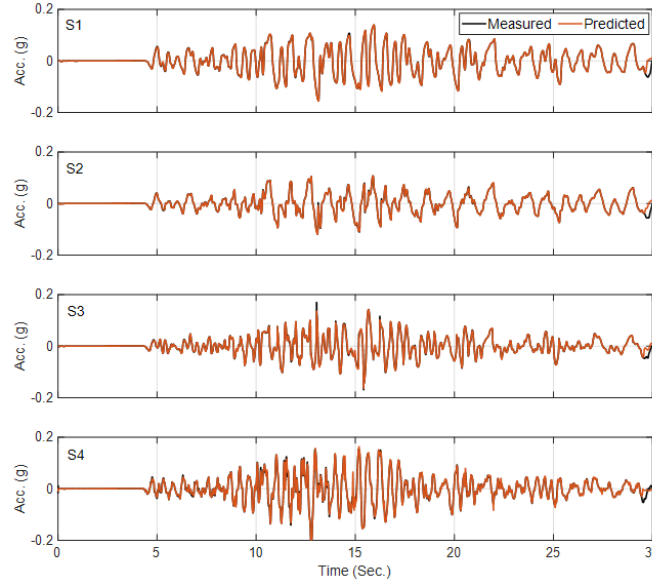


Figure 12. Comparison between measured and predicted acceleration responses in Case 3.

3.4 Case 4: Complex Domain with Unknown Incident/Outcrop Motion

The last case is the most difficult case in which the site is a complex site with unknown parameters. Also, the incident motion is unknown too. For this case, the identification method in its OO mode would not be able to simultaneously identify parameters and unknown excitation because the number of parameters is large (20 unknown parameters). So, the inverse problem is solved in two steps: In the first step, the domain is assumed fixed at the lowest instrumented level (S4) and the measured within motion is used as input excitation to identify parameters of the domain. In the second step, the incident excitation is estimated by setting parameters at their estimated values.

Error! Reference source not found. shows the variation of estimated parameters (normalized with the corresponding true values) at every iteration of the first step. As seen, the results are quite similar to those were obtained in Case 1. As seen in **Figure 14** predicted responses at sensors S1 to S3 are identical to the measured (simulated) responses. Comparison between the initial error and the final error of all 20 estimated parameters are reported in **Table 4**. As seen, this table is very similar to **Table 2**.

Now, having identified nonlinear parameters of all layers, the second step of the identification is carried out in OO mode to only estimate incident motion. In this step, the measurement at S4 is also added to the measured responses. Also, to reduce low-frequency error, both acceleration and velocity signals are used. **Figure 15** shows the comparison between exact and estimated incident motion. As seen, the estimated excitation is almost identical to the exact incident velocity motion.

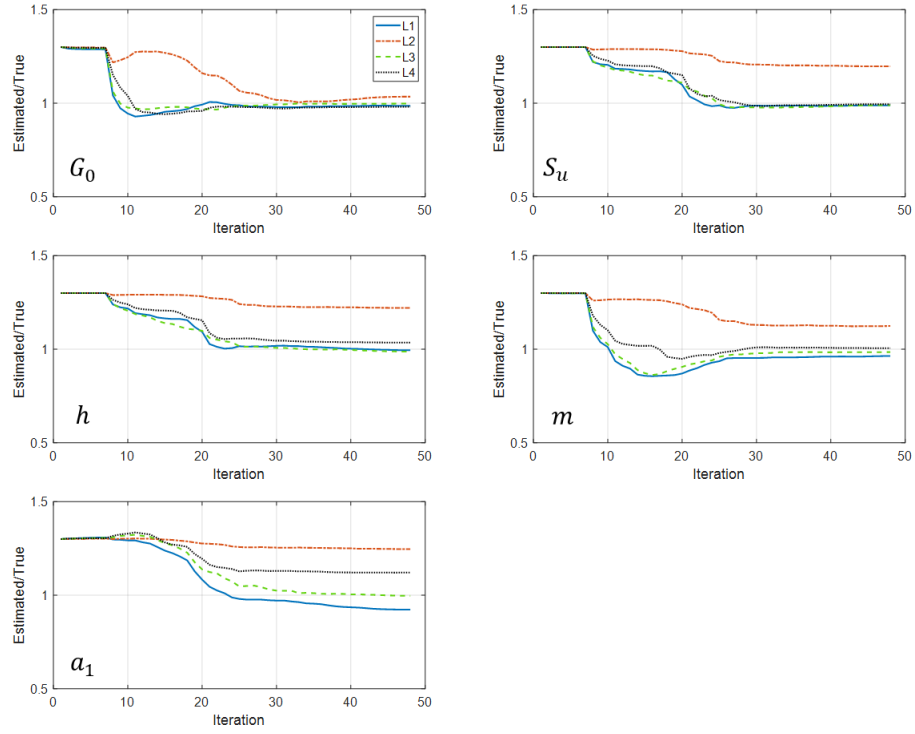


Figure 13. Identified parameters in Step 1 of Case 4 (normalized by the true values).

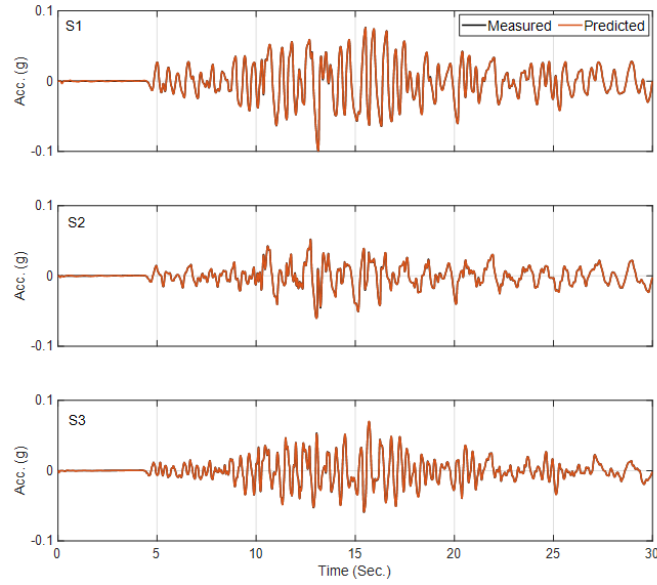


Figure 14. Comparison between measured and predicted acceleration responses in Step 1 of Case 4.

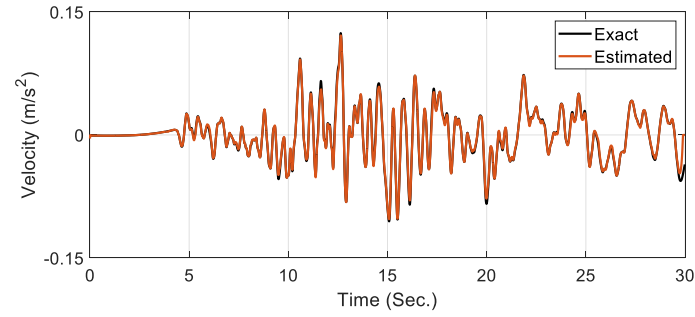


Figure 15. Comparison between the exact and estimated incident motion in Step 2 of Case 4.

Table 4. The initial and final error of parameters in Step 1 of Case 4.

Layer	Parameter	Initial Error (%)	Final Error (%)
1	G_0	+30	-1.41
	S_u	+30	-1.17
	h	+30	-0.52
	m	+30	-3.63
	a_1	+30	-7.73
2	G_0	+30	3.48
	S_u	+30	19.69
	h	+30	22.09
	m	+30	12.4
	a_1	+30	24.59
3	G_0	+30	-0.21
	S_u	+30	-1.06
	h	+30	-1.32
	m	+30	-1.53
	a_1	+30	-0.35
4	G_0	+30	-1.86
	S_u	+30	-0.51
	h	+30	3.54
	m	+30	0.55
	a_1	+30	-12.09

4 Validation Using Real Data

4.1 The Centrifuge Test Data

The centrifuge test data is precious data for the validation studies because parameters of the domain and input excitations are largely under control. Herein, we use data from a very recent centrifuge test series on buried culvert structures. The configuration of the test and the types of input excitations used to excite the domain are shown in Figure 16. The details of these tests can be found in [32]. The data from the free-field column (far from structures) under Event #10 is used here. As this is real data, a one-dimensional FE model with a three-component excitation (1D-3C) is developed in Opensees. The 1D-3C FE model, the sensor location (red circles), and the parameters of the BA model which are obtained from [33] are shown in Figure 16 too.

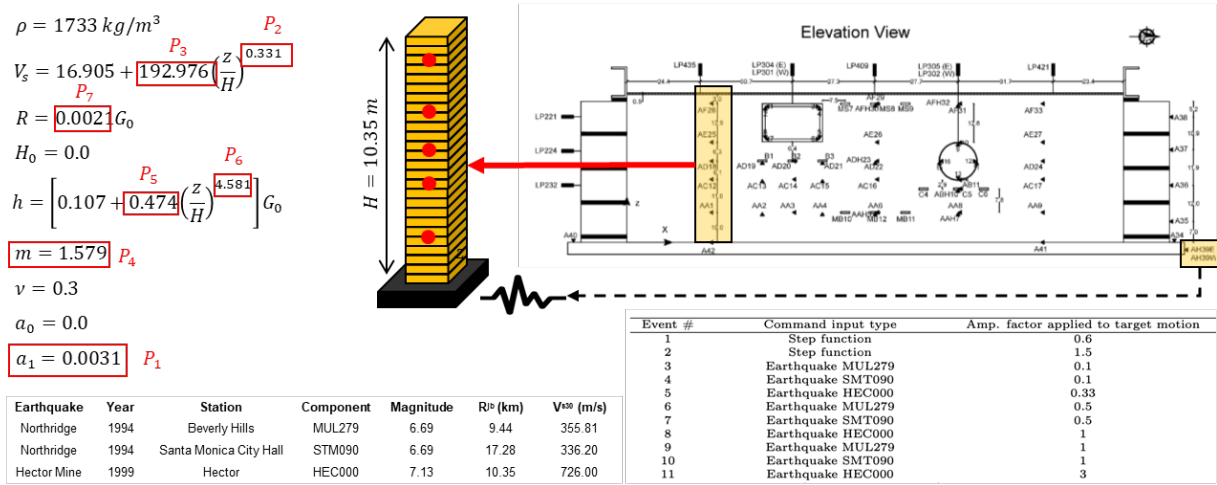


Figure 16. Centrifuge experiment.

We use this model and data to validate the single-step OO solution because the number of unknown parameters is limited. The base motion along with seven parameters specified in Figure 16 are considered as unknown parameters. We start the updating assuming a 50% initial error (with respect to the values reported in [33]) for the parameters and a 10% initial Coefficient Of Variation (COV). The results of the identification are shown in Table 5. As seen, out of these 7 parameters, Parameter 3 has a very large estimation COV showing that the problem is almost insensitive to this parameter, and the estimated value is unreliable. All other parameters are estimated with small COV, and the estimated values are reliable, and most of them are close to the considered exact values with various levels of differences, except Parameter 5, which shows a very large error. To see how the predicted responses using these values differ from the prediction using the so-called exact values Figure 17 is presented. In this figure, acceleration responses recorded during the test are shown in black, and those predicted by the “exact” and identified parameters are shown in red in the left and right columns, respectively. As seen, the responses obtained from the updated model are closer to the recorded responses. As these responses are used for the model updating, it is not surprising to see such a better prediction. However, as shown in Figure 18, the estimated base acceleration is very close to the recorded motion at the base of the shake table supporting the results of the output-only model updating carried out here.

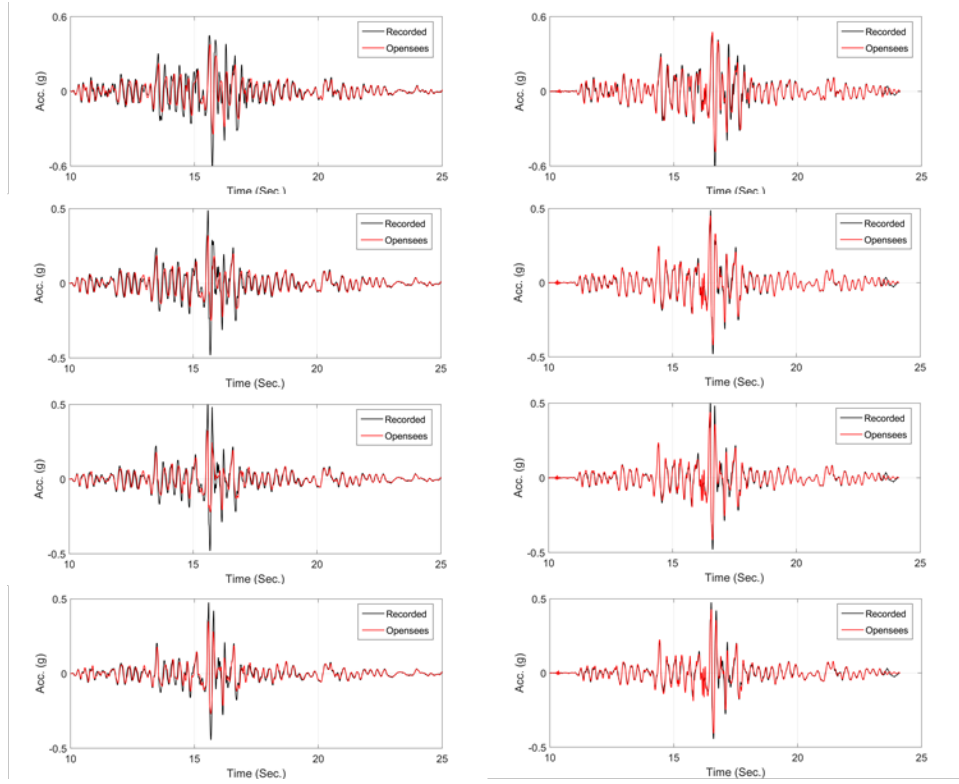


Figure 17. Comparison between recorded and predicted acceleration responses at four top sensors using considered exact (left) and identified (right) parameters.

Table 5. identification results.

Parameter	Initial Value	Final Value	Initial COV	Final COV
1	+50%	-1.4%	10%	0.0%
2	+50%	+91%	10%	0.2%
3	+50%	+50%	10%	70%
4	+50%	+7%	10%	1.0%
5	+50%	+800%	10%	3.2%
6	+50%	-33%	10%	2%
7	+50%	-13%	10%	0.0%

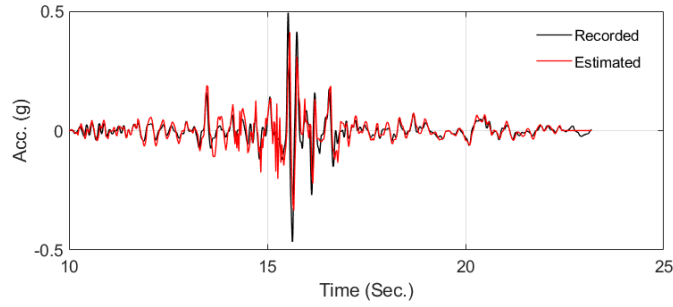


Figure 18. Comparison between exact and estimated input excitations.

4.2 The Earthquake Data From Lotung Site

The Lotung Large-Scale Seismic Tests (LSST) site is located in the North-East of Taiwan. This site was established in a seismically active region in 1985 to study seismic soil-structure interaction effects on nuclear power plants. To do so, two scaled structures were constructed by the Electric Power Research Institute (EPRI) and the Taiwan Power Company [34]. In addition to the structures, the responses of the soil were recorded in several locations on the surface and at different depths, as shown in **Figure 19**(right). Due to such dense instrumentation, the data from this site has been the subject of many studies [28], [35]–[39]. Specifically, Zeghal and Elgamal [7], [40] have extensively studied several earthquake data sets recorded at this site between 1985 to 1986 (Table 6)².

Table 6. Recorded earthquake data at the Lotung site [7], [41].

Event (1)	Date (2)	Magnitude (M_i) (3)	Epicentral distance (km) (4)	Focal depth (km) (5)	Distance to zone of energy release (km) (6)	Peak Acceleration ^a		
						EW (g) (7)	NS (g) (8)	V (g) (9)
LSST 1	9/20/85	—	—	—	—	— ^b	—	—
LSST 2	10/26/85	5.3	—	—	—	0.03	0.03	0.01
LSST 3	11/7/85	5.5	—	—	—	0.01	0.01	0.01
LSST 4	1/16/86	6.5	23.7	10.2	25.80	0.15 ^c	0.26 ^c	0.11 ^c
LSST 5	3/29/86	—	—	—	—	0.04	0.03	0.03
LSST 6	4/8/86	5.4	31.4	10.9	33.24	0.04	0.03	0.01
LSST 7	5/20/86	6.5	66.2	15.8	68.06	0.16	0.21	0.04
LSST 8	5/20/86	6.2	69.2	21.8	72.55	0.03	0.03	0.01
LSST 9	7/11/86	4.5	5.0	1.1	5.12	0.07	0.05	0.01
LSST 10	7/16/86	4.5	6.1	0.9	6.17	0.03	0.04	0.02
LSST 11	7/17/86	5.0	6.0	2.0	6.32	0.07	0.10	0.04
LSST 12	7/30/86	6.2	5.2	1.6	5.44	0.16	0.19	0.20
LSST 13	7/30/86	6.2	—	—	—	0.05	0.03	0.02
LSST 14	8/5/86	4.9	4.7	2.3	5.32	0.05	0.03	0.02
LSST 15	11/14/86	—	—	—	—	0.02	0.04	0.05
LSST 16	11/14/86	7.0	77.9	6.9	78.21	0.13	0.17	0.10
LSST 17	11/14/86	—	—	—	—	0.04	0.04	0.02
LSST 18	11/15/86	—	—	—	—	0.03	0.02	0.01

^aPeak accelerations for the DHB array including the surface FA1-5 station.
^bLSST 1 records did not include any free field motion.
^cLSST 4 records were affected by electric glitches.

Out of these 18 events, the first three events and Event No. 13 are not available. Also, the resolution of the digitized signals is relatively poor in several cases (Events No. 5, 6, 8, 9, 10, 15, 17, and 18). We also need

² Data is publicly available at <http://soilquake.net/Downholearray/Lotung/>

data with a significant level of motion to observe soil nonlinearity. Moreover, the behavior of the site must be close to 1D, so the source of the earthquake should be far from the site. Considering these criteria, events 7 and 16 are the best candidates that have been used by Borja et al. [28], [39], [42] too. The channels mostly used in previous studies and used here are FA1-5, DHB6, DHB11, DHB17, and DHB47 (see **Figure 19**(right)) which are at depths of 0, 6, 11, 17, and 47 meters, respectively. It is noteworthy to mention that Channel 47 is not available in Event No. 16, so Step 1 (IO) can only be carried out for the first 17 meters.

As the BA model is being used in this study, we model the Lotung site using the information provided by Borja et al. [28], [39]. **Figure 19**(left) shows the layered FE model of the first 47 m of the Lotung site with a fixed bottom condition (within boundary condition) and the profiles of the shear wave velocity and elastic shear modulus (The mass density profile was calculated using these two profiles). The instrumented depths are specified by red circles (the lowest level is at the fixed boundary). The parameters of the BA model of all layers are the same and taken from [42] as $R = 0.0015G_{max}$, $H_0 = 0$, $h = 0.63G_{max}$, $m = 0.97$ and the Poisson ratio is 0.48. The fundamental natural frequency of the elastic model fixed at depth 47 m obtained from the numerical model is 1.33 Hz. Note that this frequency could be different from the natural frequency of the Lotung site. The natural frequency of the model is obtained by applying a fictitious fixed boundary condition (imposing an infinite impedance contrast), but the dominant frequency observed in the recorded data could be different depending to the depth at which there is actually such significant impedance contrast [43].

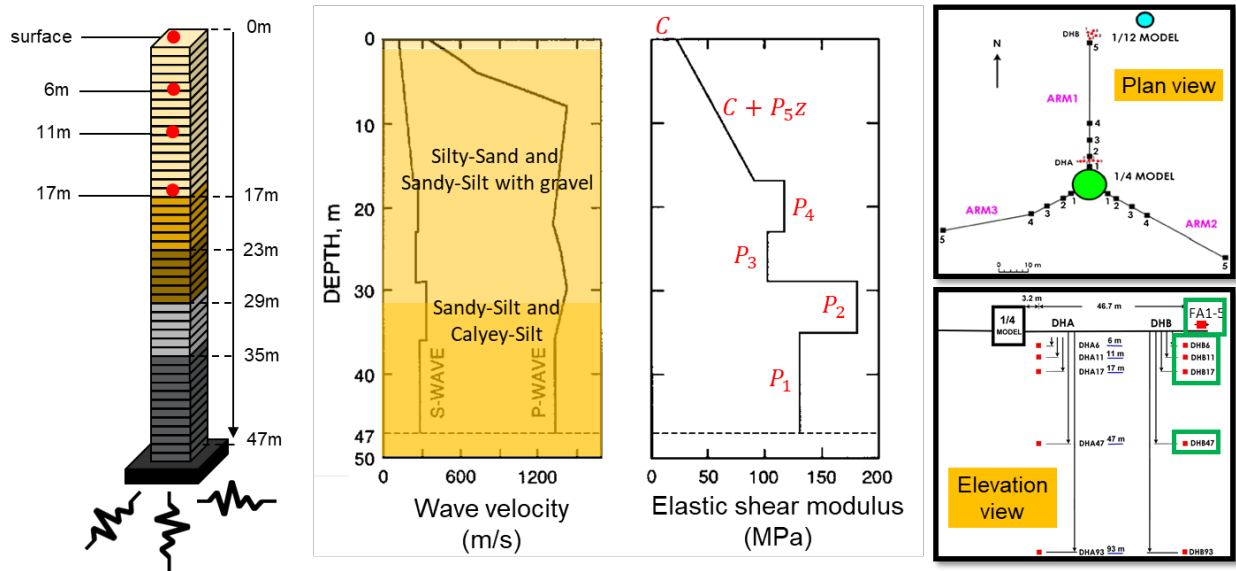


Figure 19. The FE model of the first 47 m of the Lotung site with a fixed bottom condition (left), shear wave velocity and elastic shear modulus profile (middle) [42], and Plan and elevation views of the site (right).

To set the damping parameters, Borja et al. [42] identified a dominant excitation frequency of 0.65 Hz from the recorded signal at a depth of 47 m in the LSST7 event. They assumed a 1% stiffness proportional damping resulting in a factor of 0.005. So, the same level of damping was assumed in this study whenever simulations are carried out. To make the results comparable, the same modeling and analysis assumptions are used. An element size of 1 m is used through which frequencies up to 25 Hz can be resolved. So, all recorded signals are decimated to 50 Hz. Analyses are also carried out at the same rate, but subsampling is used whenever there is a convergence issue. Similar to [42], the Hilber-Hughes-Taylor (HHT) integration method with $\alpha = -0.1$, $\beta = 0.3025$, and $\gamma = 0.6$ is employed for all analyses. The effect of pore water pressure is neglected, and all analyses are carried out in a total stress state.

For the Lotung site, the lowest instrumented level is at 47 m, and there is limited information about the layering below this level. So, we use the identification algorithm in IO mode to only estimate the parameters of the soil layers. Out of two suitable events (LSST7 and LSST16), the sensor at depth 47 m did not work in the event LSST16, so we can only use LSST7. We consider 9 updating parameters. As shown in **Figure 19**, 5 parameters (P_1 to P_5) define maximum shear modulus (G_0) of 5 layers. Four remaining parameters are P_6 to P_9 which define other nonlinear properties of soil layers using their corresponding G_0 as follows $R = P_6 G_0$, $h = P_7 G_0$, $m = P_8$, and $a_1 = P_9$. Also, for all layers it is assumed that $\nu = 0.48$, $H_0 = 0$, and $a_0 = 0.0$.

As there is no ground truth for the updating parameters, we validate the results of the identification by excluding the measurement level (depth 11 m) from model updating data. **Figure 20** shows a comparison between recorded acceleration responses at four depths and in three directions with those obtained using the model with updated parameters. Considering this is a real-life case and there could be various sources of modeling and measurement noises, the level of match is very good. Also, the observed compatibility in response prediction at depth 11 m shows that the identification results are reliable.

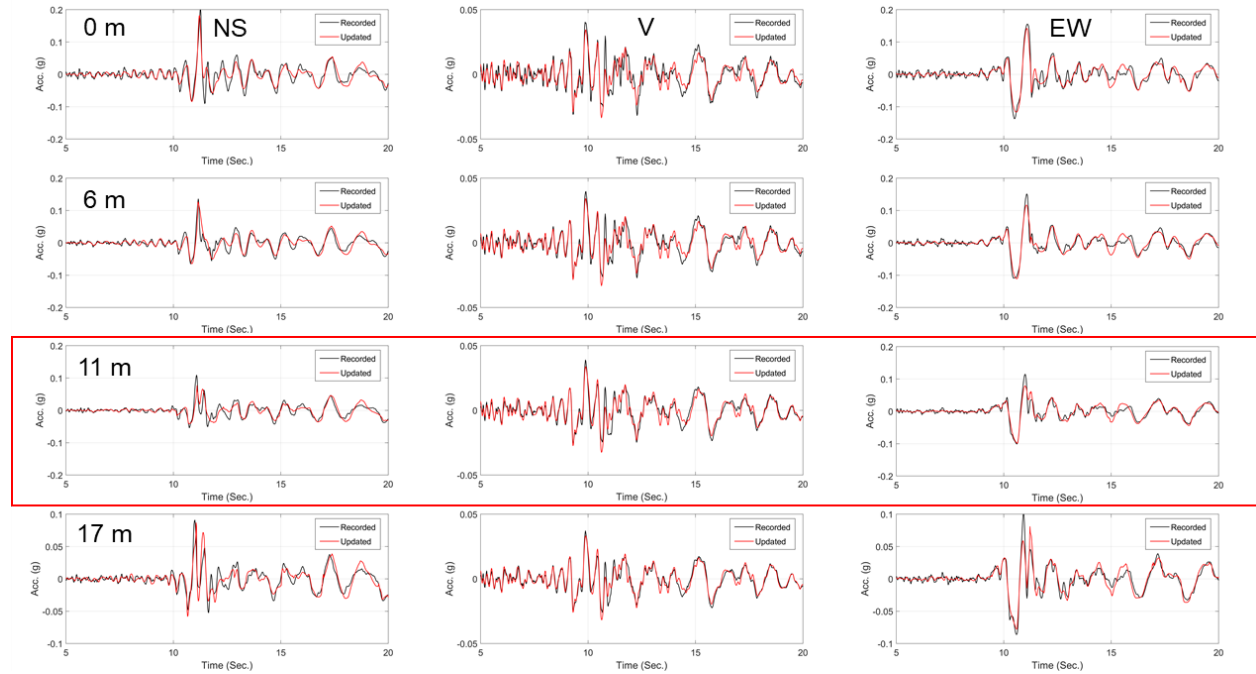


Figure 20. Comparison between recorded and predicted/updated acceleration responses in four depths and three directions. The recorded responses at depth 11 m are not used for the model updating.

5 Application to Real Earthquake Data

As a real-life application, the data from the CSMIP station 68323 is used. **Figure 21**(left) shows the instrumentation layout and the P- and S-wave velocity profiles. The idealized version of the V_s profile was taken from [44] as shown in **Figure 21**(right). This idealized profile was later more idealized into 6 layers as colored in **Figure 21**(right). By the time of this study, 8 earthquake events have been recorded by this station, which are all very weak motions. The largest event is the 2014 South Napa event in which Peak Ground Acceleration (at the surface) was about 0.03g.

The V_s profile below 35 m is not known, so we only carry out the first step (input-output) identification as was done for the Lotung site in the previous section. Five parameters for each layer (G_0, S_u, h, m, a_1) are considered as unknown parameters, which result in 30 updating parameters. **Figure 22**(left) shows the comparison between the predicted responses using the updated model and the recorded signals. The comparison between the updated, initial [44] and modified (the idealized version of the initial profile) V_s profiles are shown in Error! Reference source not found.(right). These results show that the measured V_s profile is relatively accurate although it is a little bit lower than what we obtained using earthquake data.

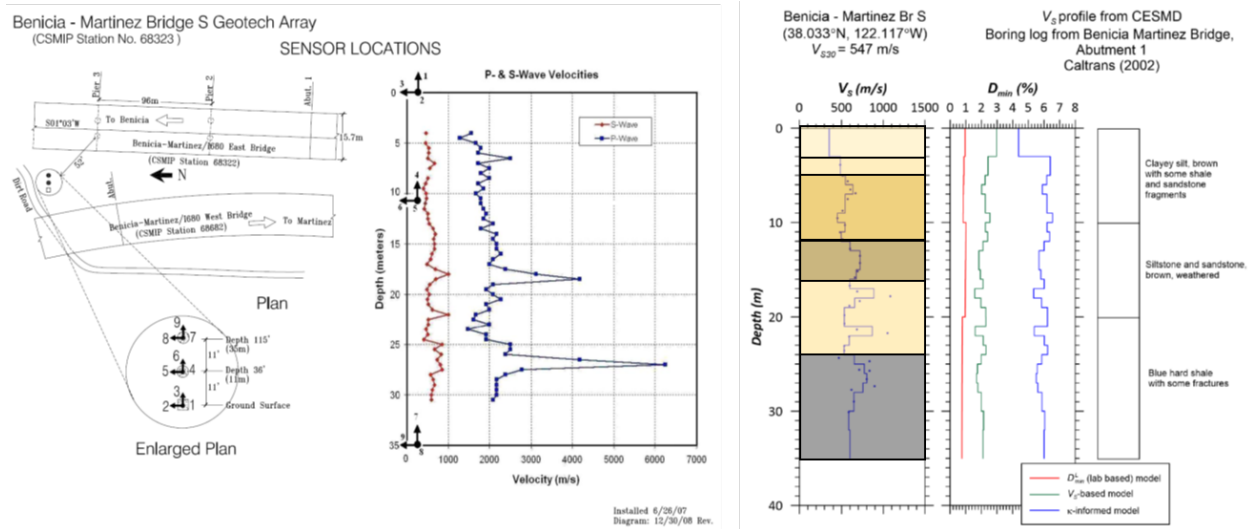


Figure 21. Benicia-Martinez Geotechnical Array. Instrumentation layout from CESMD (left), shear wave velocity, and small-strain damping profile [44].

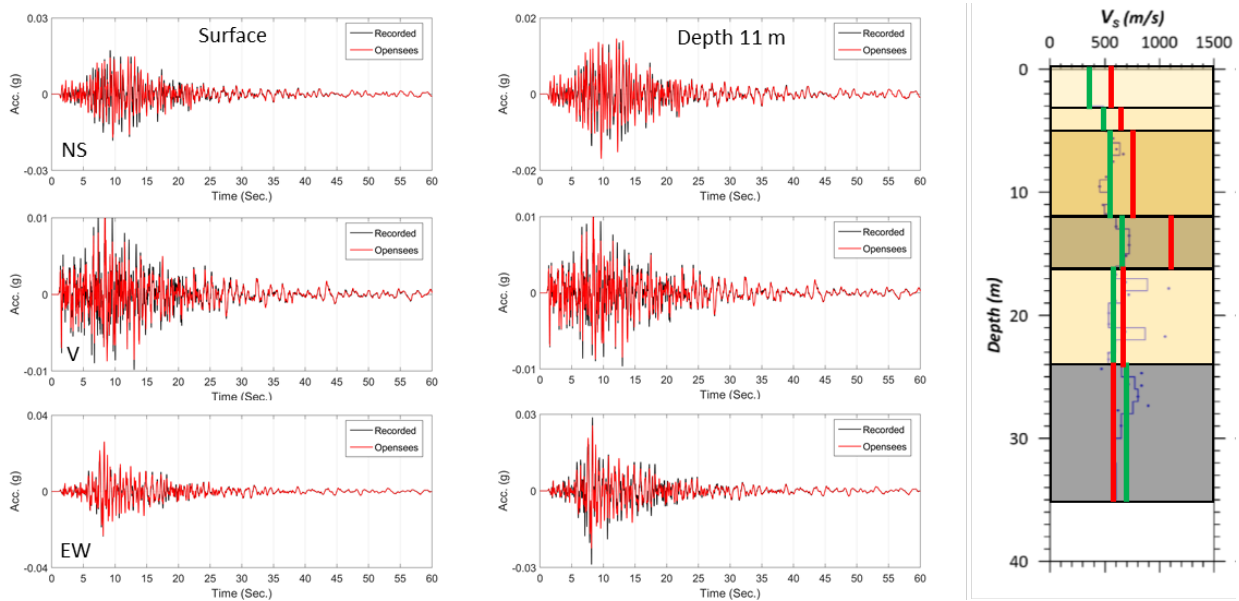


Figure 22. Left: comparison between recorded and predicted/updated acceleration responses in the South Napa 2014 earthquake. Right: Comparison between initial [44], modified/idealized, and updated V_s profile shown in blue, green, and red, respectively.

In addition to this station, we carried out the same identification for several other cases too which are not reported here for the sake of the space.

6 Conclusions

We proposed the application of stochastic filtering to estimated nonlinear soil properties from earthquake data recorded by the geotechnical arrays. Dynamic soil properties are key ingredients of analysis for predicting/assessing soil-structure interaction (SSI) and site response effects under seismic excitations. Although there are various techniques and tools to carry out forward site response analysis with various levels of complexity, there could be significant uncertainty due to the available uncertainties in nonlinear soil models and their parameters. By using the proposed framework, various inverse 1D problems can be solved to obtain a reliable estimation of the soil properties even in the absence of the incident excitation. The method was verified using synthetic examples representing various scenarios and validated using centrifuge data and data recorded in the well-known Lotung site. The method was also applied to several CSMIP Geotechnical Arrays one of them was presented in this report.

Project Data

The centrifuge test data is publicly available at DesignSafe.ci with the following address <https://doi.org/10.17603/DS2Z38Z>. Earthquake data of the Lotung site is publicly available at <http://soilquake.net/Downholearray/Lotung/>. The CSMIP data is taken from the Center for Engineering Strong Motion Data (CESMD), which a public database that can be accessed at <https://www.strongmotioncenter.org/>.

Bibliography of Publications Resulting From the Work Performed

Under the Award

No publications have resulted yet from this Award.

References

- [1] S. L. Kramer, *Geotechnical Earthquake Engineering*, vol. 6. New York: Prentice Hall, 1996.
- [2] I. M. Idriss and H. B. Seed, "Seismic Response of Horizontal Soil Layers," *J. Soil Mech. Found. Div.*, vol. 94, no. 4, pp. 1003–1034, 1968.
- [3] J. M. Roesset, "Soil amplification of earthquakes," *Numer. methods Geotech. Eng.*, pp. 639–682, 1977.
- [4] D. Park and Y. M. a. Hashash, "Soil Damping Formulation in Nonlinear Time Domain Site Response Analysis," *J. Earthq. Eng.*, vol. 8, no. 2, pp. 249–274, 2004, doi: 10.1080/13632460409350489.
- [5] I. a Beresnev and K. Wen, "Nonlinear Soil Response-A Reality?," *Bull. Seismol. Soc. Am.*, vol. 86, no. 6, pp. 1964–1978, 1996, doi: 10.1061/(ASCE)0733-9410(1996)122:9(725).
- [6] E. H. Field and K. H. Jacob, "A comparison and test of various site-response estimation techniques, including three that are not reference-site dependent," *Bull. Seismol. Soc. Am.*, vol. 85, no. 4, pp. 1127–1143, 1995.
- [7] A. W. Elgamal, M. Zeghal, H. T. Tang, and J. C. Stepp, "Lotung Downhole Array. I: Evaluation of Site Dynamic Properties," *J. Geotech. Eng.*, vol. 121, no. 4, pp. 350–362, 1995, doi: 10.1061/(ASCE)0733-9410(1995)121:4(350).
- [8] S. F. Ghahari, F. Abazarsa, C. Jeong, A. Kurtulus, and E. Taciroglu, "Blind identification of site effects and bedrock motions from surface response signals," *Soil Dyn. Earthq. Eng.*, vol. 107c, pp. 322–331, 2018.

- [9] S. F. Ghahari, F. Abazarsa, and E. Taciroglu, "Probabilistic blind identification of site effects from ground surface signals," *Bull. Earthq. Eng.*, 2017, doi: 10.1007/s10518-017-0253-0.
- [10] J.-S. Lin, "Extraction of dynamic soil properties using extended Kalman filter," *J. Geotech. Eng.*, vol. 120, no. 12, 1994, doi: 10.1061/(ASCE)0733-9410(1994)120:12(2100).
- [11] E. Şafak, "Models and methods to characterize site amplification from a pair of records," *Earthq. Spectra*, vol. 13, no. 1, pp. 97–129, 1997, doi: 10.1193/1.1585934.
- [12] R. Astroza, H. Ebrahimian, Y. Li, and J. P. Conte, "Bayesian nonlinear structural FE model and seismic input identification for damage assessment of civil structures," *Mech. Syst. Signal Process.*, vol. 93, pp. 661–687, 2017.
- [13] H. Ebrahimian, S. F. Ghahari, D. Asimaki, and E. Taciroglu, "A nonlinear model inversion to estimate dynamic soil stiffness of building structures," in *Geotechnical Special Publication*, 2018, doi: 10.1061/9780784481479.030.
- [14] H. Ebrahimian, *Nonlinear finite element model updating for nonlinear system and damage identification of civil structures*. University of California, San Diego, 2015.
- [15] C. McGann and P. Arduino, "Site response analysis of a layered soil column (total stress analysis)," *OpenSees Ex. Wiki. Univ. Washingt.*, 2010.
- [16] J. Lysmer and R. L. Kuhlemeyer, "Finite Dynamic Model For Infinite Media," *J. Eng. Mech. Div.*, vol. 95, no. 4, pp. 859–878, 1969, doi: 10.1089/dia.2007.0302.
- [17] W. B. Joyner and A. T. F. Chen, "Calculation of nonlinear ground response in earthquakes," *Bull. Seismol. Soc. Am.*, vol. 65, no. 5, pp. 1315–1336, 1975.
- [18] H. Ebrahimian, R. Astroza, J. P. Conte, and R. A. de Callafon, "Nonlinear finite element model updating for damage identification of civil structures using batch Bayesian estimation," *Mech. Syst. Signal Process.*, vol. 84, pp. 194–222, 2017, doi: 10.1016/j.ymssp.2016.02.002.
- [19] S. Haykin, *Kalman Filtering and Neural Networks*, vol. 5, no. 3. 2001.
- [20] S. J. Julier and J. K. Uhlmann, "New extension of the Kalman filter to nonlinear systems," in *Signal Processing, Sensor Fusion, and Target Recognition VI*, 1997, vol. 3068, p. 182, doi: 10.1117/12.280797.
- [21] M. Vucetic and R. Dobry, "Effect of soil plasticity on cyclic response," *J. Geotech. Eng.*, 1991, doi: 10.1061/(ASCE)0733-9410(1991)117:1(89).
- [22] R. I. Borja and A. P. Amies, "Multiaxial cyclic plasticity model for clays," *J. Geotech. Eng.*, vol. 120, no. 6, pp. 1051–1070, 1994.
- [23] M. T. Manzari and Y. F. Dafalias, "A critical state two-surface plasticity model for sands," *Geotechnique*, 1997, doi: 10.1680/geot.1997.47.2.255.
- [24] F. Pisanò and B. Jeremić, "Simulating stiffness degradation and damping in soils via a simple visco-elastic-plastic model," *Soil Dyn. Earthq. Eng.*, vol. 63, pp. 98–109, 2014, doi: 10.1016/j.soildyn.2014.02.014.
- [25] Z. Yang, A. Elgamal, and E. Parra, "Computational Model for Cyclic Mobility and Associated Shear Deformation," *J. Geotech. Geoenvironmental Eng.*, vol. 129, no. 12, pp. 1119–1127, 2003, doi: 10.1061/(ASCE)1090-0241(2003)129:12(1119).
- [26] D. C. Drucker and W. Prager, "Soil mechanics and plastic analysis or limit design," *Q. Appl. Math.*, vol. 10, no. 2, pp. 157–165, 1952, doi: 10.1090/qam/48291.
- [27] F. McKenna, "OpenSees: a framework for earthquake engineering simulation," *Comput. Sci. Eng.*, vol. 13, no. 4, pp. 58–66, 2011.
- [28] R. I. Borja, H. Y. Chao, F. J. Montans, and C. H. Lin, "Nonlinear ground response at Lotung LSST site," *J. Geotech. Geoenvironmental Eng.*, vol. 125, no. 3, pp. 187–197, 1999, doi: 10.1061/(ASCE)1090-0241(1999)125:3(187).
- [29] M. B. Darendeli, "Development of a new family of normalized modulus reduction and material damping

- curves,” 2001.
- [30] M. Arduino, P. Taciroglu, E. Bonilla, F.; Taiebat, “Development of a numerical nonlinear soil module to expand the capabilities of the SCEC BroadBand Platform,” 2019.
 - [31] V. Graizer and A. Shakal, “Analysis of some of CSMIP strong-motion geotechnical array recordings,” in *Proceedings of the International Workshop for Site Selection, Installation and Operation of Geotechnical Strong-Motion Arrays: Workshop 1, Inventory of Current and Planner Arrays*, 2004, vol. 14.
 - [32] E. Esmailzadeh Seylabi, E. Agapaki, D. Pitilakis, J. Stewart, S. Brandenberg, and E. Taciroglu, “Development of validated methods for soil-structure interaction analysis of buried structures,” *Des. Dataset*, 2017.
 - [33] E. E. Seylabi, H. Ebrahimian, W. Zhang, D. Asimaki, and E. Taciroglu, “Bayesian Estimation of Nonlinear Soil Model Parameters Using Centrifuge Experimental Data,” in *Geotechnical Special Publication*, 2018, doi: 10.1061/9780784481486.042.
 - [34] H. T. Tang, Y. K. Tang, and J. C. Stepp, “Lotung large-scale seismic experiment and soil-structure interaction method validation,” *Nucl. Eng. Des.*, 1990, doi: 10.1016/0029-5493(90)90260-5.
 - [35] X. S. Li, C. K. Shen, and Z. L. Wang, “Fully coupled inelastic site response analysis for 1986 Lotung earthquake,” *J. Geotech. Geoenvironmental Eng.*, 1998, doi: 10.1061/(ASCE)1090-0241(1998)124:7(560).
 - [36] G. Elia, M. Rouainia, D. Karofyllakis, and Y. Guzel, “Modelling the nonlinear site response at the LSST down-hole accelerometer array in Lotung,” *Soil Dyn. Earthq. Eng.*, 2017, doi: 10.1016/j.soildyn.2017.08.007.
 - [37] S. D. Glaser and L. G. Baise, “System identification estimation of soil properties at the Lotung site,” *Soil Dyn. Earthq. Eng.*, 2000, doi: 10.1016/S0267-7261(00)00026-9.
 - [38] C. Y. Chang, C. M. Mok, and H. T. Tang, “Inference of dynamic shear modulus from Lotung downhole data,” *J. Geotech. Eng.*, 1996, doi: 10.1061/(asce)0733-9410(1996)122:8(657).
 - [39] R. I. Borja, B. G. Duvernay, and C.-H. Lin, “Ground response in Lotung: total stress analyses and parametric studies,” *J. Geotech. Geoenvironmental Eng.*, vol. 128, no. 1, pp. 54–63, 2002.
 - [40] M. Zeghal, A.-W. Elgamal, H. T. Tang, and J. C. Stepp, “Lotung Downhole Array. II: Evaluation of Soil Nonlinear Properties,” *J. Geotech. Eng.*, vol. 121, no. 4, pp. 363–378, 1995, doi: 10.1061/(ASCE)0733-9410(1995)121:4(363).
 - [41] M. Zeghal, A. W. Elgamal, H. T. Tang, and J. C. Stepp, “Lotung downhole array. II: Evaluation of soil nonlinear properties,” *J. Geotech. Eng.*, 1995, doi: 10.1061/(ASCE)0733-9410(1995)121:4(363).
 - [42] R. I. Borja, C. H. Lin, K. M. Sama, and G. M. Masada, “Modelling nonlinear ground response of non-liquefiable soils,” *Earthq. Eng. Struct. Dyn.*, 2000, doi: 10.1002/(SICI)1096-9845(200001)29:1<63::AID-EQE901>3.0.CO;2-Y.
 - [43] Y. Tao and E. Rathje, “The Importance of Distinguishing Pseudoresonances and Outcrop Resonances in Downhole Array Data,” *Bull. Seismol. Soc. Am.*, 2020, doi: 10.1785/0120190097.
 - [44] K. Afshari and J. Stewart, “Implications of California vertical array data for the analysis of site response with 1D geotechnical modeling,” 2017.